Mixed halide ordering as a tool for the stabilization of Ruddlesden-Popper structures

Juraj Ovčar,[1,‡] Tik Lun Leung,[2,‡], Luca Grisanti,[1] Željko Skoko[3], Martina Vrankić,[1] Kam-Hung Low,[4] Shixun Wang,[5] Pei-Ying You,[6] Hyeyoung Ahn,[6] Ivor Lončarić[1,*], Aleksandra B. Djurišić[2,*] and Jasminka Popović[1,*]

[1] Ruđer Bošković Institute, Bijenička 54, Zagreb, Croatia

[2] Department of Physics, The University of Hong Kong, Pokfulam Road, Hong Kong

[3] Department of Physics, Faculty of Science, University of Zagreb, Bijenička 32, Zagreb, Croatia

[4] Department of Chemistry, The University of Hong Kong, Pokfulam Road, Hong Kong

[5] Department of Materials Science and Engineering and Centre for Functional Photonics, City University of Hong Kong, 83 Tat Chee Avenue, Hong Kong

[6] Department of Photonics, College of Electrical and Computer Engineering, National Yang Ming Chiao Tung University, Hsinchu 30010, Taiwan

ABSTRACT: While the constraints on the choice of organic cations are greatly relaxed for layered 2D perovskites compared to 3D perovskites, the shape of the spacer cation is still subject to limitations due to the size of the inorganic pocket between four adjacent corner-sharing octahedra. To investigate the effect of spacer cation branching on the formation of Ruddlesden-Popper (RP) structures, we performed a comprehensive investigation of structures formed using *tert*-butyl ammonium (*t*-BA). We demonstrate that in contrast to pure bromides and pure iodides, the use of mixed halides enables the formation of *t*-$BA_2PbBr_2I_2$ RP perovskite structure with the specific ordering of the bromide and iodide anions. The *t*-BA spacer, despite its branched and bulky shape that prevents its deeper penetration, is able to form significant H-bonds that lead to the stabilization of RP assembly if the inorganic pocket is designed in such a way that the bromide anions occupy terminal axial positions while iodides occupy equatorial positions. We obtain excellent agreement between experimentally determined and theoretically predicted structures using Global Optimization *via* Minima Hopping Algorithm for Layered Perovskites, illustrating the ability to predict the structure of RP perovskites and to manipulate the perovskite structure by rational design of the inorganic pocket.

INTRODUCTION

Hybrid inorganic-organic lead halide perovskites, including both three-dimensional (3D) and low-dimensional (2D and quasi-2D) perovskites, are impressing the semiconductor community with their astounding physical properties and optoelectronic applications as solar cells and light-emitting diodes (LEDs) that outperform many other materials.[1-8] Low-dimensional perovskites include the 2D and quasi-2D perovskites, which crystallize in the Ruddlesden-Popper (RP) structural type with the general formula $A'_2A_{n-1}B_nX_{3n+1}$ (where A' is the larger organic spacer cation, A is a smaller cation forming a 3D perovskite slabs ABX_3, B is a divalent metal center, X is a halide anion, while *n* is the number of perovskite sheets). These materials have attracted attention due to their improved properties compared to 3D perovskites, such as higher exciton binding energy and improved environmental stability due to the presence of spacer cations capable of locking the octahedral framework and preventing the penetration of water molecules.[9-22] Different from simple morphological size reduction where properties of ABX_3 nanostructures with sufficiently small size can be tuned by changing the size due to quantum confinement effects, the properties of RP perovskites can be tuned by changing the layer thickness, A cation, and A' spacer cation and these materials exhibit great structural diversity.[23] The size restrictions imposed by the Goldschmidt tolerance factor for 3D perovskites become greatly relaxed in the case of 2D layered perovskites, allowing spacer cations of different lengths to be incorporated between the inorganic layers, as demonstrated by Billing *et al*. who reported 2D *n*=1 structures for linear cations with up to 18 carbons.[24] While there are no restrictions on spacer length, there is still a requirement for the width; cation must fit into an inorganic pocket defined by the axial (terminal) halide anions of four adjacent corner-shared octahedra.[25] Given these requirements imposed by the dimensions of the inorganic pocket, it is obvious that the shape of the spacer cation, especially but not limited to the shape of its amino head, plays an important role in the dimensionality of the perovskite.[23] Reduced dimensionality becomes even more expected when bulky size is additionally accompanied by the limited flexibility of ammonium head. Primary ammonium spacers have been proved to be the best choice for stabilizing 2D perovskites, followed by secondary, tertiary and quaternary ammonium cations.[23] Recently, the use of the secondary ammonium cation dimethylammonium (DMA) led to the formation of the 0D perovskite $(DMA)_4PbI_6$.[26] Similar shape-related constraints were demonstrated by Kanatzidis *et al.* for the hexa- and hepta-methyleneimine spacers that formed the 1D chains of face-shared octahedra.[27]

Considering the effects that both the size and the shape of the ammonium head have on the (de)stabilization of the 2D layered structure, one might expect that the branching of the spacer cation (in the vicinity of the ammonium head) could also have a significant impact on the dimensionality of the perovskite and the resulting properties. Among the many spacer cations, the structure and optoelectronic properties of *n*-butylammonium (*n*-BA) perovskites have been studied most extensively.[28-33] As in the case of *n*-BA, *iso*-butylammonium (*i*-BA) spacer also forms a 2D layered structure.[34,35] Although promising results have been reported on the use of *tert*-butylammonium (*t*-BA) to improve solar cell performance,[36-39] there are no reported structures of perovskites based on *t*-BA. In contrast to the *n*- and *iso*-butylammonium isomers, it has been suggested that the *t*-BA cation is either incorporated into a 3D perovskite structure[36,37] or forms a 1D perovskite structure,[36] but it has also been claimed that it can form a 2D structure.[39,40] In all cases, detailed structural analysis was lacking and none of the structures have been determined.

In this work, we report the effects of branching on the dimensionality of the perovskite and show that neither bromides nor iodides with *t*-BA spacer are able to form the 2D RP structure. But more importantly, we demonstrate how a targeted rational design of an inorganic pocket can be utilized as an effective tool to achieve an RP assembly despite the branched and bulky nature of spacer cation and consequently affect the optical properties. Finally, we also demonstrate the ~~great efficiency~~ potential of the new method to predict the structure of RP perovskites.

EXPERIMENTAL SECTION

Chemicals. Lead (II) iodide (PbI_2, 99.9985%), poly(methyl methacrylate) (PMMA), toluene (anhydrous, 99.8%), dimethyl formamide (DMF, anhydrous, 99.9%) and acetonitrile (ACN, anhydrous, 99.8+%) were purchased from Alfa Aesar. Lead (II) bromide ($PbBr_2$, 98+%) and chloroform (CF, anhydrous, 99+%) were purchased from Sigma Aldrich. *Tert*-butylammonium bromide (*t*-BABr) and *tert*-butylammonium iodide (*t*-BAI) were purchased from Greatcell Solar Materials. All chemicals were used as received.

Preparation of single-crystal samples. The single-crystal samples were prepared by antisolvent-induced crystallization. Seeding solutions of pure bromide and the mixed bromide and iodide (Br:I = 1:1) compounds were

prepared by dissolving the salt in DMF (0.2 M), while that of pure iodide compound was prepared by dissolving the salts in ACN (0.05 M). The molar ratio of spacer halide and lead halide salts was 2:1. After filtering, the seeding solution was placed in a 4 ml vial which was latterly placed into a 20 ml vial containing 5 ml CF. The large vials were then capped and rested in dark. Crystallization was induced by CF diffusion into the seeding solution. After few days, single-crystals were formed in the small vial.

Preparation of thin-films. The precursor solutions for film deposition were prepared by dissolving the spacer halide and lead halide (2:1 molar ratio) in DMF (0.2 M). Quartz substrates were washed with detergent, water, acetone and isopropanol in ultrasonic bath for 10 min. Perovskite thin film was deposited by spin coating the precursor solution on substrate in 4000 rpm for 30 s. The film was annealed at 80 ºC for 10 min. PMMA layer was spin-coated on perovskite (2.5 w% in toluene) to protect the film from ambient exposure.

Characterizations. All optical measurements were performed in ambient (20 °C and 45 %RH) and the samples were taken from the glovebox immediately before the measurement. Steady state PL spectra were obtained by PDA-512 USB (Control Development Inc.) Fiberoptic Spectrometer with a HeCd laser (325 nm) as the excitation source. Diffuse-reflectance spectra of single-crystal samples were collected on a Shimadzu UV 3600 UV/Vis/NIR Spectrophotometer with an integrating sphere accessory. Film absorption spectra were obtained from an Agilent Cary 60 UV-Vis spectrometer. X-ray diffraction (XRD) patterns of the perovskite ground samples were collected with Rigaku MiniFlex 600-C Diffractometer with Co radiation. Bruker D8 VENTURE Duo FIXED-CHI X-ray diffractometer was used for crystal screening, unit cell determination, and data collection for the X-ray crystal structure. Crystals suitable for X-ray diffraction were mounted on a MiTeGen dual-thickness micro-mounts. The IμS with Mo radiation was used ($K\alpha$ = 0.71073 Å, 50 kV, 0.8 mA). Bruker AXS APEX3 (v2018.7-2) software suites were used for data collection and reduction. Absorption corrections were applied using the program SADABS. Structures were solved with XT ver.2014/5 and refined with SHELXL2018/3.[41] Hydrogen atoms were placed in idealized positions and were set riding on the respective parent atoms. All non-hydrogen atoms were refined with anisotropic thermal parameters. The structure was refined by weighted least squares refinement on F^2 to convergence. Restraints were applied on disordered parts. Molecular illustrations were prepared with MERCURY.[42] Low-temperature PL measurements were performed by using a low-vibration, closed-cycle cryostats system (attocube, AttoDRY800) with an objective lens (attocube, LT-APO/VIS, N.A.=0.82) inside the vacuum chamber. We used a pulsed solid-state laser at 355 nm (2.5 kHz, 1.1 ns) as the optical excitation source with a spot size about 5 μm. The laser power used for the power dependence of PL measurement is 100 – 2000 μW. The optical excitation and collection of emission from the samples were carried out using the same objective lens at normal incidence, and the emission signal was dispersed by a homebuilt spectrometer equipped with a TE-cooled CCD (Andor, iDus 420).

Computational details. Our algorithm called Global Optimization via Minima Hopping Algorithm for Layered Perovskites (GO-MHALP) is implemented in the Atomic Simulation Environment[43] environment. For evaluation of energies and forces we use classical potentials implemented in LAMMPS.[44] The potentials are based on the MYP classical potentials for 3D perovskites[45,46] with GAFF[47] parametrization used to provide parameters related to the organic spacers.[48,49] The nonbonding parameters for the Br-I interaction were approximated as a geometric mean of Br-Br and I-I interaction parameters. LAMMPS input files with complete lists of atomic positions and the potential parameters are given in the Supplementary data. The complete methodology for GO-MHALP is described, in detail, elsewhere[50]. DFT calculations were performed using the plane-wave basis set code Quantum Espresso[51,52] with the vdW-DF-cx exchange-correlation functional[53] and GBRV pseudopotentials.[54] The atomic positions and unit cell relaxation thresholds for the total energy change, forces on each atom and the pressure were 1 meV, 0.02 eV Å-1 and 0.5 kbar respectively. The Brillouin zone integration was performed on a Monkhorst-Pack k-point mesh[55] with a density of 5 Å. The plane-wave basis set cutoff was 816 eV. The formation energy at $T = 0$ K of various configurations was calculated from DFT energies as follows:

$$E_{\text{form}} = E(\text{t-BA}_2PbBr_x\text{I}_{4-x}) - \frac{x}{4}\text{PbBr}_2 - \frac{4-x}{4}\text{PbI}_2 \\ \frac{-x}{2}(\text{t-BA})\text{Br} - \frac{4-x}{2}(\text{t-BA})\text{I}$$

for $x = 0,2,4$.

The similarity between simulated XRD patterns is calculated using a method based on cross-correlation functions[56,57] as implemented in the PyXtal Python library[58] using the cosine weighting function with the cutoff l = 1°.

RESULTS AND DISCUSSION

Thin film samples were prepared by using *t*-BA as spacer cation and lead bromide, lead iodide and mixture of lead iodide and lead bromide as building blocks of the inorganic layer. The thin-film XRD patterns are given in **Figure S1.** The absorption and PL spectra of thin film samples are shown in **Figure 1**. From the absorption spectra, we can observe significant differences between pure and mixed halide samples. While both pure bromide and pure iodide thin films exhibit no PL, the mixed halide sample (Br/I=50:50) exhibits characteristic excitonic features in the spectra, which are commonly observed for 2D perovskites such as *n*-BA_2PbI_4.[28,59,60] To better understand the optical properties of pure halide samples, we performed low-temperature PL measurements on pure bromide thin film, since bromides exhibit better stability upon exposure to ambient compared to iodide thin films. The low-temperature PL spectra are shown in **Figure S2**. We can observe that the pure bromide samples exhibit a two-peak emission at low temperature, and that the higher energy peak is rapidly quenched. The broad low energy peak exhibits power dependence consistent with excitonic recombination, as shown in **Figure S2b**, and the temperature dependences of the peak positions and PL intensity are more consistent with those previously observed in alkylammonium lead halides with structure different from 2D Ruddlesden-Popper materials.[56] Furthermore, activation energies determined from the Arrhenius equation (**Figure S3b**) are in the range 60-80 meV, which is lower than that commonly observed for 2D RP perovskites, and similar to other organo-lead halides with different connectivity of the lead halide octahedra.[56] While $(t\text{-BA})_2PbBr_2I_2$ exhibited improved ambient stability compared to pure halide samples, it is known that mixed halide perovskites including the 2D materials can be susceptible to photosegregation.[61-63] Therefore, it is worthwhile to examine the stability of $(t\text{-BA})_2PbBr_2I_2$ under illumination. The photoluminescence spectra measured after different times of laser illumination and the absorption spectra measured for different times of solar illumination are shown in **Figure 2.**

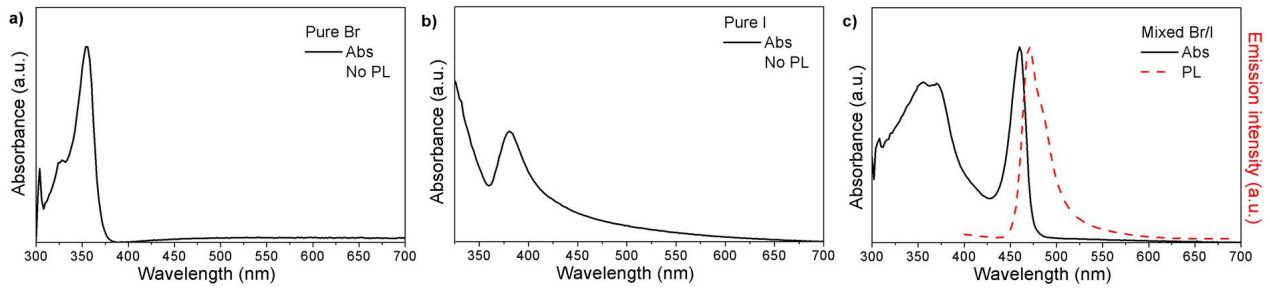

Figure 1. Absorption spectra and corresponding PL spectra of thin film samples for **a)** pure bromide compound **b)** pure iodide compound and **c)** mixed bromide/iodide (50:50) compound.

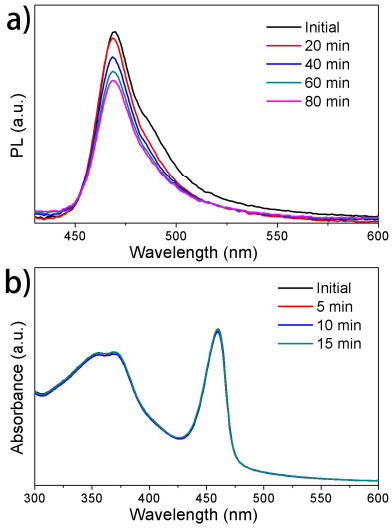

Figure 2 a) PL spectra as a function of excitation time under 325 nm laser excitation; b) absorption spectra for different times under simulated solar illumination of PMMA protected $(t\text{-BA})_2PbBr_2I_2$ thin films.

From **Figure 2**, we can observe that $(t\text{-BA})_2PbBr_2I_2$ exhibits significant resistance to photosegregation; no observable shifts in peak positions in the PL spectra of $(t\text{-BA})_2PbBr_2I_2$ over a period of 80 minutes of continuous laser excitation have been observed, demonstrating an exceptional stability. The phenomenon is known to depend on the spacer cation, since 2D perovskites with different spacer cations exhibit significant difference in susceptibility to photosegregation.[61,63] Since the ion diffusion responsible for photosegregation is dependent, among other others, on the crystal structure (including the direction),[62] it is necessary to examine the structure of $(t\text{-BA})_2PbBr_2I_2$ in more detail, both experimentally and computationally.

To tackle the reasons of different optical behavior of prepared samples, the structural features of pure- and mixed-halide samples have been explored by minima hopping algorithm (MH) algorithm dubbed Global Optimization by Minima Hopping for Layered Perovskites (GO-MHALP) developed by us. Minima hopping is a class of algorithms used for crystal structure prediction that involves a thorough exploration of the potential energy surface (PES) of a system by alternating molecular dynamics (MD) with local structure optimizations (relaxations), where combined criteria are used to determine whether the optimized structure is accepted as a newly found local minimum.[64-66] A complete description of the methodology is given in a separate work.[50] Input files containing classical potential parameters are given in the Supplementary data. **Figure S4** shows starting structures for GO-MHALP with idealized inorganic frames and approximate positions of *t*-BA for the following scenarios:

a) all PbX_6 positions occupied by bromides,
b) all PbX_6 positions occupied by iodides,
c1) axial positions of PbX_6 octahedra occupied by iodides and equatorial positions occupied by bromides,
c2) axial positions of PbX_6 octahedra occupied by bromides and equatorial positions occupied by iodides,
c3) all halide positions alternately occupied by bromides and iodides.

The output of GO-MHALP is a list of found local minima for each starting structure. The possibility of considering different minima is important due to polymorphous nature of these materials.[67] The lowest energy minimum for each configuration is relaxed with DFT and the formation energy of the relaxed structure is computed. As shown in **Table S1**, negative formation energy is obtained only for the c2) configuration. This suggests that the formation of RP structure not only requires the use of mixed halides, but also that bromides and iodides must o ccupy specific positions within the inorganic layer. Stability of such arranged mixed halides and instability of pure halide phases can be also understood from values of strain in these structures compared to 3D counterparts with methylammonium cation. As can be seen in **Table S2,** c2) configuration has strain of only 0.29%, compared to strain of 3.93% for configuration a) and 2.64% in configuration b).

On the experimental side, single-crystal X-ray diffraction structure determination of pure bromide and iodide compounds, indeed, revealed that the prepared compounds do not form a layered structures typical of Ruddlesden-Popper perovskites, as predicted by the GO-MHALP. Iodide compound contains 1D inorganic polymer chains built up from $[Pb_2I_6]^{2+}$ units while the bromide compound contains inorganic layers constructed by $[Pb_2I_5]^{+}$ building blocks. Single-crystal data, data collection and refinement parameters are summarized in **Table 1**. In order to evaluate the stability of prepared compounds under exposure to ambient condition, single-crystals samples were also ground and recorded on PXRD (**Figure S5**). Structural analysis showed that ground single-crystals contain an additional impurity, 1D-hydrated structure as reported in the work by Correa-Baena.[68] Similar impurity was observed for bromide compound; it is reasonable to assume that two unidentified diffraction reflections at 8.8 and 17.8 ° belong to the hydrated structure, similar as in the case of iodide. Changes in the single-crystal samples of pure halide compounds after grinding can be clearly observed, as shown in **Figure S6**. It should also be noted that the iodide sample is more unstable, especially on ambient exposure. Unlike pure halide compounds, ground single-crystals of mixed halide compound did not show any additional phases.

Table 1. Single crystal data, data collection and refinement parameters for $(t\text{-BA})Pb_2Br_5$, $(t\text{-BA})_2PbBr_2I_2$ and $(t\text{-BA})PbI_3$

	$(t\text{-BA})Pb_2Br_5$	$(t\text{-BA})_2PbBr_2I_2$	$(t\text{-BA})PbI_3$
Empirical formula	Br_5Pb_2, $C_4H_{12}N$	Br_2I_2Pb, $2(C_4H_{12}N)$	I_6Pb_2, $2(C_4H_{12}N)$
Formula weight	888.08	769.10	1324.07
Temperature/K	300(2)	298(2)	302(2)
Crystal system	Monoclinic	Monoclinic	Monoclinic
Space group	$P2_1$	$P2_1/c$	$P2_1$
a/Å	10.3847(19)	13.0080(14)	10.0969(14)
b/Å	8.5375(15)	8.7484(9)	7.9180(11)
c/Å	8.5372(15)	8.7588(10)	16.375(2)
α/°	90	90	90
β/°	90.006(5)	109.374(3)	90.006(3)
γ/°	90	90	90
Volume/Å^3	756.9(2)	940.30(18)	1309.1(3)
Z	2	2	2
m/mm^{-1}	35.374	16.485	19.910
ρ_{calc} g/cm^3	3.897	2.716	3.359
F(000)	764	688	1136
Crystal size/mm^3	0.207 × 0.089 × 0.026	0.154 × 0.133 × 0.017	0.127 × 0.062 × 0.018
Radiation	Mo $K\alpha$ (λ = 0.71073 Å)	Mo $K\alpha$ (λ = 0.71073 Å)	Mo $K\alpha$ (λ = 0.71073 Å)
2θ(max)/ °	64.184	58.956	52.766
Index ranges	-15 ≤h≤ 15, -12 ≤k≤ 12, -12 ≤l≤ 12	-18 ≤h≤ 17, -12 ≤k≤ 12, -12 ≤l≤ 12	-12 ≤h≤ 12, -9 ≤k≤ 9, -20 ≤l≤ 20
Data/restraints/parameters	5176/70/133	2600/0/82	5321/222/162
Restrained goodness of fit	0.974	1.053	0.970
R_{int}	0.1595	0.0770	0.1496
Final R indexes [I≥2s(I)]	R_1 = 0.0788, wR_2 = 0.1173	R_1 = 0.0565, wR_2 = 0.1398	R_1 = 0.0603, wR_2 = 0.1288

Final *R* indexes [all data]	R_1 = 0.1565, wR_2 = 0.1463	R_1 = 0.0862, wR_2 = 0.1569	R_1 = 0.1766, wR_2 = 0.1704
Largest diff. peak/hole/e Å^{-3}	1.623/-1.730	1.101/-1.298	1.136/-1.247
CCDC number	2094380	2091431	2099767

The (*t*-BA)PbI_3 crystallizes in a non-centrosymmetric monoclinic $P2_1$ space group with one $[Pb_2I_6]^{2-}$ unit and two $(CH_3)_3NH_3^+$ cations in the asymmetric unit. The 1D-polymeric chain shown in **Figure 3a**, which consist of face-shared octahedra under the 1-2 F_{346} F_{346} notation[69] exhibits a pseudo S_6 symmetry. Chains, running parallel to the *b*-direction, are mutually bridged *via* *t*-BA cations that form weak hydrogen bonds between methyl groups and iodide atoms from Pb-octahedra, forming a loose intermolecular sheet in the *ab* plane (**Figure 3b**). Additional weak H-bond is formed between iodide atoms and the ammonium group. Both $(CH_3)_3NH_3^+$ cations are disordered; one is treated as a two-part disorder (major part 63%, minor part 37%) and the second one is treated as a three-part disorder (major part 44%, minor parts 36% and 20%).

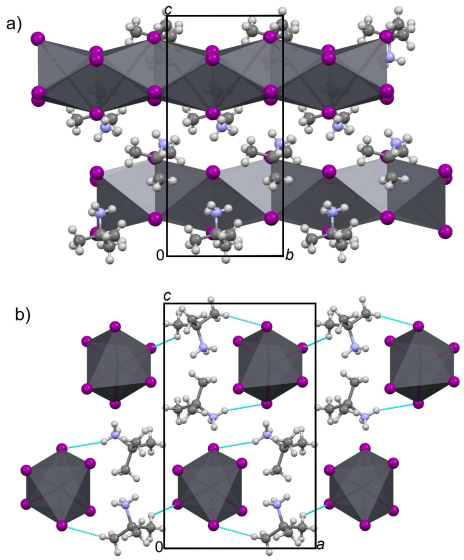

Figure 3. The 1D structure of (*t*-BA)PbI_3 in **a)** *bc* plane and **b)** *ac* plane. Iodide is given in purple, lead in dark grey, carbon in light grey, nitrogen in pale blue while hydrogen atoms are shown in white. Hydrogen bonds are shown as dashed turquoise lines. Organic cations are disordered between several positions; only the major part is shown.

The (*t*-BA)Pb_2Br_5 crystallizes in a non-centrosymmetric monoclinic $P2_1$ space group with one $[Pb_2Br_5]^-$ unit and one $(CH_3)_3NH_3^+$ cation in the asymmetric unit. As shown in **Figure 4a**, inorganic 2D layers are separated by a monolayer of *t*-BA cations. Considering Pb···Br contacts up to ~ 3.39 Å (**Figure 4b**), coordination spheres of lead can be described as the $PbBr_8$ bicapped trigonal prisms that are connected in a face-shared manner thus forming a 2D inorganic layer. Trigonal pyramidal geometry is found for bromide atoms (Br1-Br4), where three Pb atoms at located at the corners of a trigonal base and bromide is located at the apex. Unlike Br1 to Br4 atoms, Br5 atom is experiencing a square planar geometry. Such a geometry of inorganic layers also was reported for $Cs_2Pb_2Br_5$.[70,71] Inorganic layers are mutually interconnected *via* H-bonds between ammonium groups and bromide, as well as weaker ones involving bromide and methyl groups. Similarly, as in the case of iodide compound, $(CH_3)_3NH_3^+$ cation is disordered over two positions (major part 53%, minor part 47%).

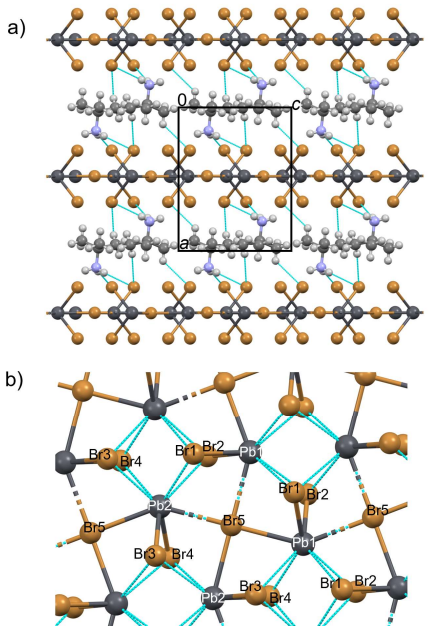

Figure 4. a) The 2D structure of (*t*-BA)$_2Pb_2Br_5$ in *ac* plane and **b)** inorganic layer consisting of $PbBr_8$ bicapped trigonal prisms (caps at Br5 atoms). Bromide is given in dark orange, lead in dark grey, carbon in light grey, nitrogen in pale blue while hydrogen atoms are shown in white. Hydrogen bonds are shown as dashed turquoise lines. Organic cations are disordered between several positions; only the major part is shown.

Finally, the (*t*-BA)$_2PbBr_2I_2$ crystallizes in a centrosymmetric monoclinic $P2_1/c$ space group, in a typical 2D Ruddlesden-Popper arrangement with the inorganic layers consisting of PbX_6 (X = I and Br) octahedra, connected in a corner-shared manner, separated by the bilayer of spacer *t*-BA molecules as shown in **Figure 4**. When the quantitative criterion of relative shift of layers (LSF) is applied to (*t*-BA)$_2PbBr_2I_2$, the value of LSF equals to [0.49, 0.49]; indicating that the structure belongs to the pure RP type.[72] It is particularly important to notice that halides are ordered within the inorganic layer; all axial positions in PbX_6 are occupied by bromides, exclusively, while iodides are located solely on the equatorial positions. The ordering of anions (pseudohalide-thiocyanates and iodides) is also found in $[MA]_2Pb(SCN)_2I_2$.[73] The tendency of smaller halide to occupy the axial position was also found in Dion-Jacobson perovskite (2meptH2)$PbBr_{4-x}Cl_x$ for x=1.4.[74] As shown in **Figure 4a**, all three hydrogen atoms from the ammonium group participate in the formation of H-bonding; two hydrogen atoms are bonded to axial (terminal) bromide from neighbouring $PbBr_2I_4$ octahedra while the third one is connected to the equatorial iodide atom. In the structure of (*t*-BA)$_2PbBr_2I_2$ no disorder was found for organic spacer cation while both types of halide atoms are disordered over two positions (major part 98%, minor part 2%).

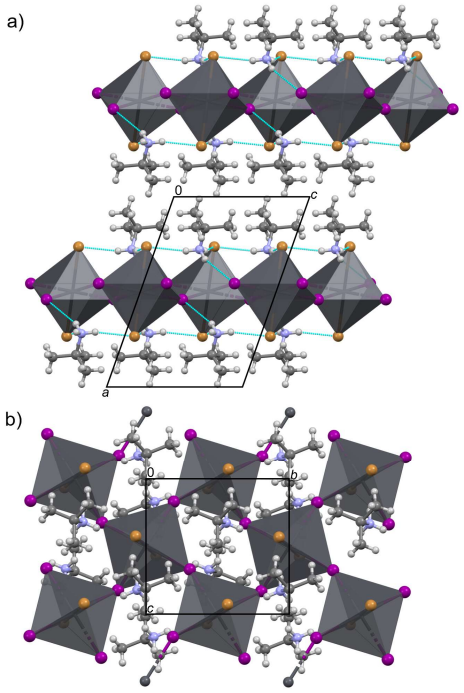

Figure 5. The 2D structure of $(t\text{-BA})_2PbBr_2I_2$ in **a)** *ac* plane and **b)** *bc* plane. Bromide is given in dark orange, iodide in purple, lead in dark grey, carbon in light grey, nitrogen in pale blue while hydrogen atoms are shown in white. Hydrogen bonds are shown as dashed turquoise lines. Halide atoms are disordered between two positions, only the major part is shown.

The stability of 2D perovskites, or the ability to form such a 2D assembly at all, is strongly influenced by the bonding strength, *i.e.* strength of the interactions between the inorganic layer and the organic bilayer. Spacers with bulky groups substituted on the N atom of the amino head are known to destabilize the 2D structure; while the stabilization of 2D structures is easily achieved with a primary ammonium spacer, the use of secondary and tertiary ammonium cations often leads to a further reduction to 1D or 0D assemblies.[23] Our work shows that like many secondary ammonium cations, the branched *tert*-isomer of the primary BA cation cannot form either bromide or iodide-based 2D RP structures due to the bulky substituents on the *α*-carbon in the vicinity of the ammonium head. To explain the underlying reasons, it is necessary to keep in mind that the stability of 2D perovskites is conditioned by the ability of H-bonds formation between halide anions and the ammonium head of the spacer cation. However, at the same time, the spacer cation must fit into an inorganic pocket defined as a cavity formed by four corner-shared PbX_6 octahedra in the *ab* layer. This means that the inorganic pocket must be large enough to accommodate the spacer at its equilibrium penetration depth (defined as the average distance of the N atoms to the terminal halide atoms plane), which is determined by the nature and size of the halides and their interactions with the organic cation. According to the diagram of Mitzi *et. al.*[75] that shows Pb-X-Pb angles versus penetration depth there is a strong correlation between the penetration depth and the average equatorial Pb-X-Pb angle as the equatorial halides X move out of the plane toward the amino heads to form a hydrogen bond. Although the diagram shown in the report Mitzi *et. al.*[75] summarizes many different perovskite structure published until 2017, we additionally performed a new quest to include more recent structures as well as to increase the number of structures having a lower range of penetration depths. Both the Cambridge structural database (CCDC/CSD)[76] and the Database from Laboratory of new materials for solar energetics at Lomonosov Moscow State University[77] were used for structure search; the dependence of Pb-X-Pb angles versus penetration depth is shown in **Figure 6.**

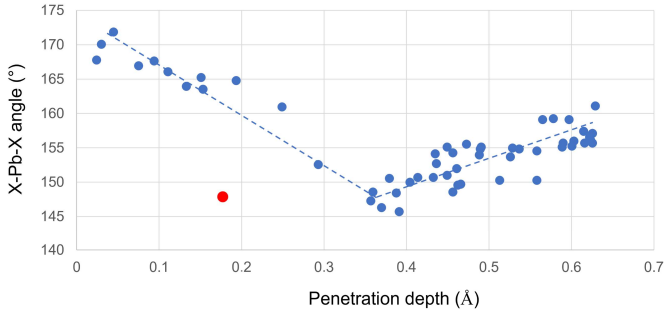

Figure 6. Pb−X−Pb bond angle dependence on the organic cation penetration for literature-reported pure halide perovskites (blue dots).[78-115] The data for $(t\text{-BA})_2PbBr_2I_2$ is represented by red dot. Dashed lines are only guidelines for the eye.

For $(t\text{-BA})_2PbBr_2I_2$, we found that average Pb-I-Pb angle is ~148 °, while the penetration depth of *t*-BA cation is ~0.177 Å. Based on the above dependence, the angle at the depth of ~0.177 Å is expected to be considerably less deformed than the one we observe, and should be >160 °, suggesting that only a rather weak hydrogen bonding would exist between equatorial halide and ammonium group. On the other hand, the penetration at an angle of ~148 ° is expected to be much deeper than observed, and should amount to >0.37 Å. Indeed, this implies that the use of mixed halides significantly alters the established dependence that is valid for pure halide perovskites. We herein propose that the specific ordering of bromides at the axial (terminal) positions and iodides at the equatorial positions plays a crucial role that enables *t*-BA to form a 2D perovskite in the case of mixed halides, based on the following arguments:

(i) the occupation of the terminal axial positions by smaller bromides leads to the spacer cation being positioned closer to the equatorial plane compared to the situation if the terminal positions were occupied by larger iodides (assuming in both cases a hypothetical penetration of 0 Å). This also means that H-bonds can be formed for shallower penetration depths.

(ii) the occupation of equatorial positions by larger iodides requires a smaller deformation of the Pb-I-Pb angle for the formation of H-bonds compared to a hypothetical case where smaller bromides would occupy equatorial positions.

Table 2 gives comparison of H-bond distances found in mixed halide *t*-BA structure with those found in pure iodide- and bromide-based RP structures with *n*-BA[78,114] and *iso*-BA[115,116] spacers. We can observe that *n*-BA and *iso*-BA isomers in pure bromide and pure iodide structures penetrate deep into the inorganic pocket, ranging from 0.476 – 0.589 Å, unlike in the case of the mixed *t*-BA structure. We also observe that even though *t*-BA is positioned very shallow within the inorganic pocket, which is imposed by its branched and bulky shape, nevertheless it forms H-bonds of similar strengths to those in *n*- and *iso*-BA structures.

Table 2. H-bond distances in mixed halide *t*-BA structure and pure iodide- and bromide-based RP structures with *n*-BA[74,114] and *iso*-BA[115,116] spacers

	$(n\text{-BA})PbI_4$[78]	$(iso\text{-BA})PbI_4$[115]	$(t\text{-BA})PbBr_2I_2$
d(N-H···I1$_{eq}$)/Å	3.619	3.817 3.682	3.839
penetration depth/Å	0.589	0.545	0.177
	$(n\text{-BA})PbBr_4$[114]	$(iso\text{-BA})PbBr_4$[116]	$(t\text{-BA})PbBr_2I_2$
d(N-H···Br1$_{ax}$)/Å	3.394 3.409	3.439 3.436	3.347 3.367
penetration depth/Å	0.537	0.476	0.177

It has to be noticed that above discussion is based on the major part (98%) that is present in the structure of $(t\text{-BA})_2PbBr_2I_2$. If one considers the minor part (halide position Br1B and I1B), changes in hydrogen bonding and geometry of PbX_6 octahedra can be observed, as expected. The minor part is still able to form H-bond with ammonium head, however only one interaction is formed (d(N-H···Br1B$_{ax}$)= 3.569 Å). On the other hand, Pb-I-Pb angle is not significantly affected; the angle Pb-I1-Pb amounts to ~148 ° while Pb-I1B-Pb angle is ~147 °. Penetration depth defined by Br1B atom positions is ~0.213 Å, thus similar to that defined by Br1 atoms. Of course, without solid-state NMR measurements, the additional presence of dynamic disorder, that is often found in metal halide perovskites, cannot be excluded.[117]

To critically evaluate the implementation of GO-MHALP for the prediction of 2D RP perovskite structures, a comparison of the experimentally deter-

mined single-crystal structure of $(t\text{-BA})_2PbBr_2I_2$ with the following structures was carried out:

i) the idealized structure relaxed with DFT.

ii) the global energy minimum structure predicted by GO-MHALP and relaxed with DFT.

Figure 7a shows the XRD patterns simulated from the experimentally determined single-crystal structure (given in red) while the patterns simulated from the structures *i*) and *ii*) are given in green and blue, respectively. Even a quick visual inspection of simulated XRD patterns reveals excellent agreement between the experimentally determined $(t\text{-BA})_2PbBr_2I_2$ structure and that predicted by GO-MHALP and refined with a DFT relaxation. Quantitatively (see Computational details), the similarities between the simulated XRD patterns of the experimentally determined structure and structures *i*) and *ii*) are 51.61% and 96.7%, respectively. The same is obvious from **Figure 7b** where the experimental and relaxed global minimum structures are shown in an overlapping manner. **Figures 7c** and **7d** depict structures in more detail; it can clearly be seen that structural features, such as the *in-plane* tilting, Pb-I-Pb distances, as well as the H-bonding motives, found by theory and experiment are in an excellent agreement. On the other hand, as shown in **Figure 7e**, the idealized structure relaxed with DFT obviously differs, significantly, in terms of atomic positions. Also, a set of typical structural descriptors were used to additionally analyses and compare the experimental structure with structures predicted with and without GO-MHALP algorithm (**Table 3**). While average bond distances and octahedral volume are similar for all three structures, distortion index *D*, bond angle variance σ^2, in-plane distortion and interlayer *d*-spacing clearly point out the structural similarity between experimental structure and model obtained with GO-MHALP algorithm.

Table 3. Typical structural descriptors comparing the experimental structure with structures predicted with and with-out GO-MHALP algorithm

	Experimental single crystal structure	Structure with GO-MHALP	Structure without GO-MHALP
Average bond length (Å)	3.13	3.16	3.16
Octahedral volume (Å^3)	40.93	41.83	39.75
Distortion index, *D*	0.034	0.035	0.045
Quadratic elongation	1.005	1.005	1.042
Bond angle variance, σ^2	8.1	9.1	122.4
Average *in-plane* distortion (°)	148.3	143.9	165.15
Interlayer *d*-spacing (Å)	12.27	12.34	11.44

The energy (as given by DFT) of the relaxed ideal structure is higher by ~0.590 eV per formula unit compared to the relaxed GO-MHALP obtained global minimum, showing that the DFT optimization of the ideal structure got stuck in a local minimum. Therefore, the benefit of GO-MHALP is twofold: *i*) it gives an indication of system stability and *ii*) it can provide unbiased input structures for DFT optimizations which result in realistic structures. Recently, a machine learning aiming to predict whether a given spacer is able or not to form 2D perovskite in case of pure iodide materials was reported.[118] Classification is based on the so-called steric effect index (STEI) and eccentricity (Ec) of spacer. For *t*-BA spacer, with STEI=1.375 and Ec=2, machine learning predicts the ability of *t*-BA to form 2D perovskite. However, our experimental single-crystal study clearly shows that a 2D perovskite is not formed for *t*-BA-based lead iodide, as correctly predicted by our GO-MHALP algorithm.

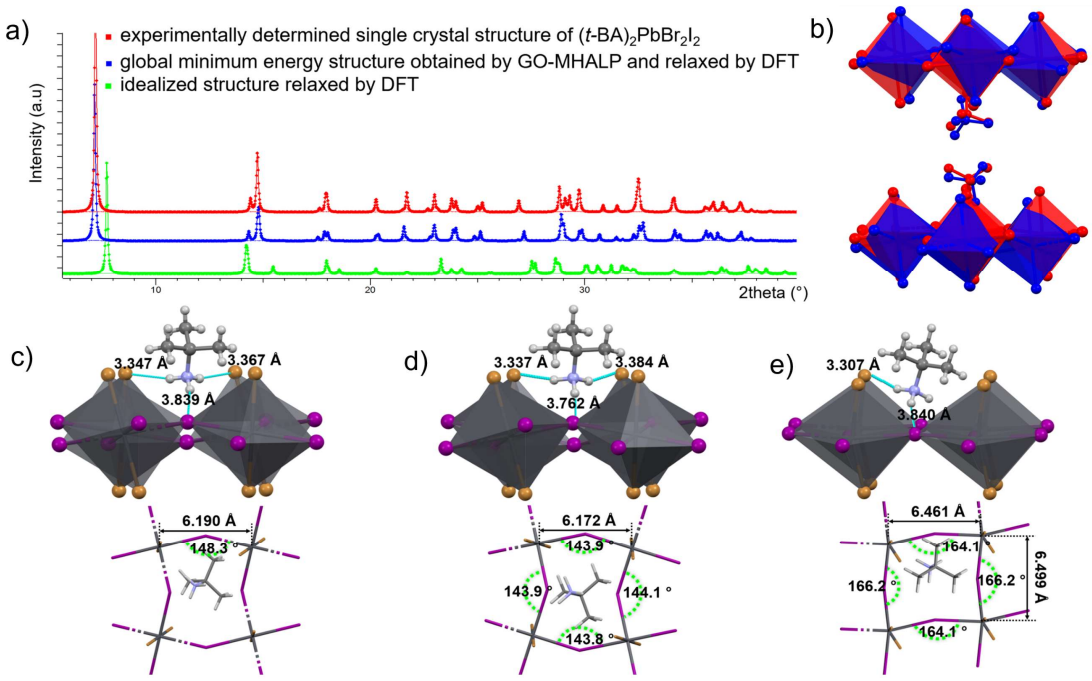

Figure 7. **a)** XRD patterns simulated from the experimental single-crystal structure and those predicted with and without GO-MHALP. **b)** Single-crystal structure (red) and global minimum energy structure predicted by GO-MHALP (blue) shown in an overlapping manner. Hydrogen atoms are omitted for clarity. Structural features of **c)** experimental structure and those predicted **d)** with GO-MHALP and **e)** without GO-MHALP. Bromide is given in dark orange, iodide in purple, lead in dark grey, carbon in light grey, nitrogen in pale blue while hydrogen atoms are shown in white. Hydrogen bonds are shown as dashed turquoise lines.

CONCLUSIONS

Based both on experimental and computational studies, we found that for pure iodides and pure bromides, RP structure could not be formed since the inorganic pocket between adjacent corner-sharing octahedra is not large enough to accommodate the *t*-BA spacer at equilibrium penetration depth. However, mixed halides are able to form a RP perovskite, which is attributed to the specific arrangement of bromide and iodide anions; such halide ordering facilitates the formation of strong hydrogen bonds at shallow penetration depth. The experimentally determined single-crystal structure is in excellent agreement with theoretical predictions obtained by the GO-MHALP algorithm, showcasing the capability of the algorithm for accurate prediction of the layered perovskite structure.

To our knowledge, $(t\text{-BA})PbBr_2I_2$ is the first 2D hybrid organic-inorganic mixed-halide perovskite crystallizing in Ruddlesden-Popper structural type whose structure has been exactly determined from the single-crystal diffraction data. It will be particularly interesting to determine, once further studies are published, whether such a specific arrangement of halides proves to be a typical feature of 2D mixed halide perovskites or whether it is a response to the geometrical requirements imposed

by the branched organic cation. In any case, it is important to further explore the implications of our results, such as the possibility of synthesizing 2D perovskites with bulky and branched organic cations, which often prevent the stabilization of 2D arrangements, by using the mixed halides.

Finally, it should be also noted that specific halide ordering in (*t*-BA)$PbBr_2I_2$ hinders migration and photosegregation thus opening up possibilities for designing photosegregation-resistant perovskites.

ASSOCIATED CONTENT

Supporting Information. XRD patterns of ground single-crystals, PL analysis of thin films, photos of single crystal samples before and after grinding, GO-MHALP input and output structures, potential energies per formula unit of minima found with GO-MHALP and relaxed with DFT for mixed configurations. CIFs corresponding to (*t*-BA)Pb_2Br_5, (*t*-BA)$_2PbBr_2I_2$ and (*t*-BA)PbI_3. LAMMPS input files that contain both the structure information and the corresponding classical potentials. This material is available free of charge via the Internet at http://pubs.acs.org.

AUTHOR INFORMATION

Corresponding Authors

Jasminka Popović: jpopovic@irb.hr, Aleksandra B. Djurišić: dalek@hku.hk , Ivor Lončarić: ivor.loncaric@irb.hr

Author Contributions

‡T. L. L. and J. O. contributed equally to this work. T. L. L. prepared the samples and performed characterization of thin film samples. T. L. L. and S. W. collected optical data at room temperature, while P. Y. Y. and H. A. measured and analysed variable temperature photoluminescence and time resolved photoluminescence. T. L. L and A. B. D. interpreted optical results. J. O. conducted the computational analysis. L. G. contributed to the analysis of computational results. K.-H. L. solved the structures from single crystal data. J. P. Ž. S. and M. V. analyzed and interpreted structural results. I. L. designed the computational part of study. J. P. and A. B. D. designed the whole study, analyzed and interpreted results and wrote the manuscript.

Notes

The authors declare no competing financial interest.

ACKNOWLEDGMENT

This work was supported by the PZS-2019-02-2068 project financed by the *"Research Cooperability"* Program of the Croatian Science Foundation and European Union from the European Social Fund under the Operational Programme Efficient Human Resources 2014-2020, the Seed Funding for Basic Research and Seed Funding for Strategic Interdisciplinary Research Scheme of the University of Hong Kong, RGC GRF projects 17301520, RGC CRF project 7035-20G, NSFC project 6207032617. The authors thank The University of Hong Kong's University Development Fund and the Dr. Hui Wai Haan Fund for funding the Bruker D8 VENTURE X-ray diffractometer.

REFERENCES

1. Yoo, J. J.; Seo, G.; Chua, M. R.; Park, T. G.; Lu, Y.; Rotermund, F.; Kim, Y. K.; Moon, C. S.; Jeon, N. J.; Correa-Baena, J. P. *et al.* Efficient perovskite solar cells via improved carrier management. *Nature* **2021**, *590*, 587–593.
2. Kim, Y.-H.; Kim, S.; Kakekhani, A.; Park, J.; Park, J.; Lee, Y.-H.; Xu, H.; Nagane, S.; Wexler, R. B.; Kim, D.-H. *et al.* Comprehensive defect suppression in perovskite nanocrystals for high-efficiency light-emitting diodes. *Nat. Photonics* **2021**, *15*, 148–155.
3. Grancini, G.; Nazeeruddin, M. H. Dimensional tailoring of hybrid perovskites for photovoltaics *Nat. Rev. Mater.* **2019,** *4*, 4−22.
4. Wang, R.; Mujahid, M.; Duan, Y.; Wang, Z-K.; Xue, J.; Yang, Y. A review of perovskites solar cell stability. *Adv. Funct. Mater.* **2019**, *29*, 1808843.
5. Arora, N.; Dar, M. I.; Hinderhofer, A.; Pellet, N.; Schreiber, F.; Zakeeruddin, S. M.; Grätzel, M. Perovskite solar cells with CuSCN hole extraction layers yield stabilized efficiencies greater than 20%. *Science* **2017**, *358*, 768−771.
6. Yang, W. S.; Park, B.-W.; Jung, E. H.; Jeon, N. J.; Kim, Y. C.; Lee, D. U.; Shin, S. S.; Seo, J.; Kim, E. K.; Noh, J. H *et al.* Iodide management in formamidinium-lead-halide-based perovskite layers for efficient solar cells. *Science* **2017**, *356*, 1376−1379.
7. Cao, Y.; Wang, N.; Tian, H.; Guo, J.; Wei, Y.; Chen, H.; Miao, Y.; Zou, W.; Pan, K.; He, Y. *et al.* Perovskite light-emitting diodes based on spontaneously formed submicrometre−scale structures. *Nature* **2018**, *562*, 249−253.
8. Lin, K.; Xing, J.; Quan, L. N.; de Arquer, F. P. G.; Gong, X.; Lu, J.; Xie, L.; Zhao, W.; Zhang, D.; Yan, C. *et al.* Perovskite light-emitting diodes with external quantum efficiency exceeding 20%. *Nature* **2018**, *562*, 245−248.
9. Mao, L. L; Stoumpos, K. C.; Kanatzidis, M. G. Two-dimensional hybrid halide perovskites: principles and promises. *J. Am. Chem. Soc.* **2019**, *141*, 1171−1190.
10. Liu, X. K.; Gao, F. Organic–inorganic hybrid Ruddlesden-Popper perovskites: an emerging paradigm for high-performance light-emitting diodes. *J. Phys. Chem. Lett.* **2018**, *9*, 2251−2258.
11. Quan, L. N.; deArquer, F. P. G.; Sabatini, R. P.; Sargent, E. H. Perovskites for light emission. *Adv. Mater.* **2018**, *30*, 1801996.
12. Stranks, S. D.; Hoye, R. L. Z.; Di, D.; Friend, R. H.; Deschler, F. The physics of light emission in halide perovskite devices. *Adv. Mater.* **2018**, *30*, 1803336.
13. Wang, N.; Cheng, L.; Ge, R.; Zhang, S.; Miao, Y.; Zou, W.; Yi, C.; Sun, Y.; Cao, Y.; Yang, R. *et al.* Perovskite light-emitting diodes based on solution-processed self-organized multiple quantum wells. *Nat. Photonics* **2016**, *10*, 699−704.
14. Yang, X.; Zhang, X.; Deng, J.; Chu, Z.; Jiang, Q.; Meng, J.; Wang, P.; Zhang, L.; Yin, Z.; You, J. Efficient green light-emitting diodes based on quasi-two-dimensional composition and phase engineered perovskite with surface passivation. *Nat. Commun.* **2018**, *9*, 570.
15. Quan, L. N.; Zhao, Y.; deArquer, F. P. G.; Sabatini, R.; Walters, G.; Voznyy, O.; Comin, R.; Li, Y.; Fan, J. Z.; Tan, H. *et al.* Tailoring the energy landscape in quasi-2D halide perovskites enables efficient green-light emission. *Nano Lett.* **2017**, *17*, 3701−3709.
16. Tsai, H.; Nie, W.; Blancon, J. C.; Stoumpos, C. C.; Soe, C. M. M.; Yoo, J.; Crochet, J.; Tretiak, S.; Even, J.; Sadhanala, A. *et al.* Stable light-emitting diodes using phase-pure Ruddlesden-Popper layered perovskites. *Adv. Mater.* **2018**, *30*, 1704217.
17. Xing, G.; Wu, B.; Wu, X.; Li, M.; Du, B.; Wei, Q.; Guo, J.; Yeow, E.K. L.; Sum, T. C.; Huang, W. Transcending the slow bimolecular recombination in lead-halide perovskites for electroluminescence. *Nat. Commun.* **2016**, *8*, 14558.
18. Chin, X. Y.; Perumal, A.; Bruno, A.; Yantara, N; Velduis, S. A.; Martinez-Sarti, L.; Chandran, B.; Chirvony, V.; Lo, A. S. Z.; So, J. *et al.* G. Self-assembled hierarchical nanostructured perovskites enable highly efficient LEDs via an energy cascade. *Energy Environ. Sci.* **2018**, *11*, 1770−1778.
19. Yuan, M.; Quan, L. N.; Comin, R.; Walters, G.; Sabatini, R.; Voznyy, O.; Hoogland, S.; Zhao, Y.; Beauregard, E. M.; Kanjanaboos, P. *et al.* Perovskite energy funnels for efficient light-emitting diodes. *Nat. Nanotechnol.* **2016**, *11*, 872−877.
20. Byun, J. W.; Cho, H. C.; Wolf, C.; Jang, M.; Sadhanala, A.; Friend, R. H.; Yang, H. C.; Lee, T. W. Efficient visible quasi−2D perovskite light-emitting diodes. *Adv. Mater*. **2016**, *28*, 7515.
21. Yantara, N.; Bruno, A.; Iqbal, A.; Jamaludin, N. F.; Soci, C.; Mhaisalkar, S.; Mathews, N. Designing efficient energy funneling kinetics in Ruddlesden-Popper perovskites for high-performance light-emitting diodes. *Adv. Mater*. **2018**, *30*, 1800818.
22. Williams, O. F.; Gau, Z.; Hu, J.; Yan, L.; You, W.; Moran, A. M. Energy transfer mechanisms in layered 2D perovskites. *J. Chem. Phys.* **2018**, *148*, 134706.

23. Li, X.; Hoffman J. M.; Kanatzidis, M. G. The 2D halide perovskite rulebook: how the spacer influences everything from the structure to optoelectronic device efficiency. *Chem. Rev.* **2021**, *121*, 2230–2291.
24. Billing, D. G.; Lemmerer, A. Synthesis, characterization and phase transitions of the inorganic-organic layered perovskite-type hybrids $[(C_nH_{2n+1}NH_3)_2PbI_4]$ (n = 12, 14, 16 and 18). *New J. Chem.* **2008**, *32*, 1736−1746.
25. Saparov, B.; Mitzi, D. B. Organic–inorganic perovskites: structural versatility for functional materials design. *Chem. Rev.* **2016**, *116*, 4558−4596.
26. Wang, Y.; Tang, Z.; Liu, C.; Jiang, J.; Liu, W.; Zhang, B.; Gao, K.; Cai, H.-L.; Wu, X. Room temperature ferroelectricity and blue photoluminescence in zero dimensional organic lead iodine perovskites. *J. Mater. Chem. C* **2021**, *9*, 223−227.
27. Mao, L.; Guo, P.; Kepenekian, M.; Hadar, I.; Katan, C.; Even, J.; Schaller, R. D.; Stoumpos, C. C.; Kanatzidis, M. G. Structural diversity in white-light-emitting hybrid lead bromide perovskites. *J. Am. Chem. Soc.* **2018,** *140*, 13078−13088.
28. Stoumpos, C. C.; Cao, D. H.; Clark, D. J.; Young, J.; Rondinell, J. M.; Jang, J. I.; Hupp, J. T.; Kanatzidis, M. G. Ruddlesden–Popper hybrid lead iodide perovskite 2D homologous semiconductors. *Chem. Mater.* **2016**, *28,* 2852−2867.
29. Gong, X.; Voznyy, O.; Jain, A.; Liu, W.; Sabatini, R.; Piontkowski, Z.; Walters, G.; Bappi, G.; Nokhrin, S.; Bushuyev, O. *et al.* Electron-phonon interaction in efficient perovskite blue emitters. *Nat. Mater.* **2018,** *17,* 550−556.
30. Wang, Z.; Wang, F.; Sun, W.; Ni, R.; Hu, S.; Liu, J.; Zhang, B.; Alsaed, A.; Hayat, T. Tan, Z. Manipulating the trade−off between quantum yield and electrical conductivity for high-brightness quasi-2D perovskite light-emitting diodes. *Adv. Funct. Mater.* **2018**, *28*, 1804187.
31. You, M.; Wang, H.; Cao, F.; Zhang, C.; Zhang, T.; Kong, L.; Wang, L.; Zhao, D.; Zhang, J.; Yang, X. Improving efficiency and stability in quasi-2D perovskite light-emitting diodes by a multifunctional LiF interlayer. *ACS Appl. Mater. Interfaces* **2020**, *12*, 43018−43023.
32. Meng, F.; Liu, X.; Chen, Y.; Cai, X.; Li, M.; Shi, T.; Chen, Z.; Chen, D.; Yip, H. L.; Ramanan, C *et al.* Co-interlayer engineering toward efficient green quasi-two-dimensional perovskite light-emitting diodes. *Adv. Funct. Mater.* **2020**, *30*, 1910167.
33. Yan, J.; Croes, G.; Fakharuddin, A.; Song, W.; Heremans, P.; Chen, H.; Qiu, W. Exploiting two-step processed mixed 2D/3D perovskites for bright green light emitting diodes. *Adv. Opt. Mater.* **2019**, *7*, 1900465.
34. Hoffman, J. M.; Malliakas, C. D.; Sidhik, S.; Hadar, I.; McClain, R.; Mohite, A. D.; Kanatzidis, M. G. Long periodic ripple in a 2D hybrid halide perovskite structure using branched organic spacers. *Chem. Sci.* **2020**, *11*, 12139−12148.
35. Wang, Z.-X.; Liao, W.-Q.; Ye, H.-Y.; Zhang, Y. Sequential structural transitions with distinct dielectric responses in a layered perovskite organic-inorganic hybrid material: $[C_4H_9N]_2[PbBr_4]$. *Dalton Trans.* **2015**, *44,* 20406−20412.
36. Bu, T.; Li, J.; Huang, W.; Mao, W.; Zheng, F.; Bi, P.; Hao, X.; Zhong, J.; Chengabe, Y. B.; Huang F. J. Surface modification via self-assembling large cations for improved performance and modulated hysteresis of perovskite solar cells. *Mater. Chem. A* **2019,** *7*, 6793−6800.
37. Liang, C.; Zhao, D.; Li, P.; Wu, B.; Gu, H.; Zhang, J.; Goh, T. W.; Chen, S.; Chen, Y.; Sha, Z. *et al.* Simultaneously boost diffusion length and stability of perovskite for high performance solar cells, *Nano Energy* **2019**, *59*, 721−729.
38. Liu, X.; He, J.; Wang, P.; Liu, Y.; Xiao, J.; Ku, Z.; Peng, Y.; Huang, F.; Cheng, Y.-B.; Zhong, J. Fabrication of efficient and stable perovskite solar cells in high-humidity environment through trace-doping of large-sized cations. *ChemSusChem* **2019**, *12,* 2385−2392.
39. Ramirez, D.; Schutt, K.; Wang, Z.; Pearson, A. J.; Ruggeri, E.; Snaith, H. J.; Stranks, S. D.; Jaramillo F. Layered mixed tin-lead hybrid perovskite solar cells with high stability. *ACS Energy Lett.* **2018**, *3*, 2246−2251.
40. Zhou, N.; Zhang, Y.; Huang, Z.; Guo, Z.; Zhu, C.; He, J.; Chen, Q.; Sun, W.; Zhou H. Mobile media promotes orientation of 2D/3D hybrid lead halide perovskite for efficient solar cells. *ACS Nano* **2021**, *15*, 8350−8362.
41. Sheldrick, G. M. SHELXT - integrated space-group and crystal-structure determination. *Acta Cryst.* **2015**, *A71*, 3−8.
42. Macrae, C. F.; Bruno, I. J.; Chisholm, J. A.; Edgington, P. R.; McCabe, P.; Pidcock, E.; Rodriguez-Monge, L.; Taylor, R.; van de Streek, J.; Wood, P.A. Mercury CSD 2.0 - new features for the visualization and investigation of crystal structures. *J. Appl. Cryst.* **2008**, *41*, 466–470.
43. Larsen, A. H. The atomic simulation environment - a python library for working with atoms. *Phys. Condens. Matter.* **2017**, *29*, 273002.
44. Plimpton, S. Fast parallel algorithms for short-range molecular dynamics. *J. Comput. Phys.* **1995**, *117*, 1–19. https://www.lammps.org.
45. Mattoni, A.; Filippetti, A.; Saba, M. I.; Delugas, P. Methylammonium rotational dynamics in lead halide perovskite by classical molecular dynamics: the role of temperature. *J. Phys. Chem. C* **2015**, *119*, 17421–17428.
46. Hata, T.; Giorgi, G.; Yamashita, K.; Caddeo, C.; Mattoni, A. Development of a classical interatomic potential for $MAPbBr_3$. *J. Phys. Chem. C* **2017**, *121*, 3724–3733.
47. Wang, J.; Wolf, R. M.; Caldwell, J. W.; Kollman, P. A.; Case, D. A. Development and testing of a general amber force field. *J. Comput. Chem.* **2004**, *25*, 1157–1174.
48. Fridriksson, M. B.; van der Meer, N.; de Haas, J.; Grozema, F. C. Tuning the structural rigidity of two-dimensional Ruddlesden-Popper perovskites through the organic cation. *J. Phys. Chem. C* **2020**, *124*, 28201–28209.
49. Shi, E.; Yuan, B.; Shiring, S. B.; Gao, Y.; Akriti; Guo, Y.; Su, C.; Lai, M.; Yang, P.; Kong, J *et al.* Two-dimensional halide perovskite lateral epitaxial heterostructures. *Nature* **2020**, *580*, 614–620.
50. Ovčar, J.; Grisanti, L.; Popović, J., Lončarić, I.; Djurišić A. B. Crystal structure prediction of two-dimensional lead halide perovskites, **2021**, submitted as *Supporting Information for Review Only*.
51. Giannozzi, P.; Baroni, S.; Bonini, N.; Calandra, M.; Car, R.; Cavazzoni, C.; Ceresoli, D.; Chiarotti, G. L.; Cococcioni, M.; Dabo, I. *et al.* QUANTUM ESPRESSO: A modular and open-source software project for quantum simulations of materials. *J. Phys. Condens. Matter* **2009**, *21,* 395502.
52. Giannozzi, P.; Andreussi, O.; Brumme, T.; Bunau, O.; Buongiorno Nardelli, M.; Calandra, M.; Car, R.; Cavazzoni, C.; Ceresoli, D.; Cococcioni, M. *et al.* Advanced capabilities for materials modelling with QUANTUM ESPRESSO. *J. Phys.: Condens. Matter* **2017**, *29*, 465901.
53. Hyldgaard, P.; Berland, K.; Schröder, E. Interpretation of van der Waals density functionals, *Phys. Rev. B* **2014**, *90*, 075148.
54. Garrity, K. F.; Bennett, J. W.; Rabe, K. M.; Vanderbilt, D. Pseudopotentials for high-throughput DFT calculations. *Comput. Mater. Sci*. **2014**, *81*, 446–452.
55. Monkhorst, H. J.; Pack, J. D. Special points for Brillouin-zone integrations. *Phys. Rev. B* **1976**, *13*, 5188–5192.
56. Gelder, R. De; Wehrens, R.; Hageman J. A.; A Generalized Expression for the Similarity of Spectra: Application to Powder Diffraction Pattern Classification. *J. Comput. Chem.* **2001**, *22*, 273–289.
57. Habermehl, S.; Mörschel, P.; Eisenbrandt, Hammer, S. M.; Schmidt, M. U. Structure determination from powder data without prior indexing, using a similarity measure based on cross-correlation functions. *Acta Cryst.* **2014**, *B70*, 347–359.
58. Fredericks, S.; Parrish, K.; Sayre, D.; Zhu, Q. PyXtal: A Python library for crystal structure generation and symmetry analysis. *Comput. Phys. Commun.* **2021**, *261*, 107810.
59. Lin, C.-W.; Liu, F.; Chen, T.-Y.; Lee, K.-H.; Chang, C.-K.; He, Y.; Leung, T. K.; Ng, A. M. C; Hsu, C.-H.; Popović, J. *et al.* Structure-dependent photoluminescence in low-dimensional ethylammonium, propylammonium, and butylammonium lead

iodide perovskites. *ACS Appl. Mater. Interfaces* **2020**, *12,* 5008–5016.
60. Cortecchia, D.; Neutzner, S.; Kandada, A. R. S.; Mosconi, E.; Meggiolaro, D.; De Angelis, F.; Soci, C.; Petrozza, A. Broadband emission in two-dimensional hybrid perovskites: the role of structural deformation. *J. Am. Chem. Soc.* **2017**, *139*, 39–42.
61. Cho, J.; Mathew, P. S.; DuBose, J. T.; Kamat, P. V. Photoinduced Halide Segregation in Ruddlesden-Popper 2D Mixed Halide Perovskite Films. *Adv Mater*. **2021**, 33, e2105585.
62. Nah, Y.; Allam, O.; Kim, H. S.; Choi, J. I.; Kim, I. S.; Byun, J.; Kim, S. O.; Jang, S. S.; Kim, D. H. Spectral Instability of Layered Mixed Halide Perovskites Results from Anion Phase Redistribution and Selective Hole Injection. *ACS Nano* **2021**, *15*, 1486−1496.
63. Mathew, P. S.; DuBose, J. T.; Cho, J.; Kamat, P. V. Spacer Cations Dictate Photoinduced Phase Segregation in 2D Mixed Halide Perovskites. ACS *Energy Lett.* **2021**, *6*, 2499–2501.
64. Goedecker, S. Minima hopping an efficient search method for the global minimum of the potential energy surface of complex molecular systems. *J. Chem. Phys.* **2004**, *120*, 9911–9917.
65. Amsler, M.; Goedecker, S. Crystal structure prediction using the minima hopping method. *J. Chem. Phys.* **2010**, *133*, 224104.
66. Peterson, A. A. Global optimization of adsorbate–surface structures while preserving molecular identity. *Top. Catal.* **2014**, *57*, 40–53.
67. Zhao, X.-G.; Dalpian, G. M.; Wang Z.; Zunger, A, Polymorphous nature of cubic halide perovskites, *Phys. Rev. B* **2020**, *101*, 155137
68. Hartono, N T. P.; Sun, S.; Gélvez-Rueda, M. C.; Pierone, P. J.; Erodici, M. P.; Yoo, J.; Wei, F.; Bawendi, M.; Grozema, F. C.; Sher, M. et al. The effect of structural dimensionality on carrier mobility in lead-halide perovskites. *J. Mater. Chem. A*, **2019**, *7*, 23949–23957.
69. Wong, W. P. D.; Hanna, J. V.; Grimsdale, A. C. The classification of 1D perovskites. *Acta Cryst.* **2021**, *B77*, 408–415.
70. Wang, K.-H.; Wu, L.; Lei, L.; Yao, H.-B.; Qian, H.-S.; Yu, S.-H. Large-scale synthesis of highly luminescent perovskite-related $CsPb_2Br_5$ nanoplatelets and their fast anion exchange. *Angew. Chem., Int. Ed.* **2016**, *55*, 8328–8332.
71. Li, G.; Wang, H.; Zhu, Z.; Chang, Y.; Zhang, T.; Song, Z.; Jiang, Y. Shape and phase evolution from $CsPbBr_3$ perovskite nanocubes to tetragonal $CsPb_2Br_5$ nanosheets with an indirect bandgap. *Chem. Commun.* **2016**, *52*, 11296–11299.
72. Tremblay, M. H.; Bacsa, J.; Zhao, B.; Pulvirenti, F.; Barlow, S.; Marder, S. R. Structures of $(4\text{-}Y\text{-}C_6H_4CH_2NH_3)_2PbI_4$ {Y = H, F, Cl, Br, I}: Tuning of Hybrid Organic Inorganic Perovskite Structures from Ruddlesden–Popper to Dion–Jacobson Limits. *Chem. Mater.* **2019**, *31*, 6145–6153.
73. Dang, Y.; Liu, G.; Song, J.; Meng, L.; Sun, Y.; Hu, W.; Tao, X. Layered Perovskite $(CH_3NH_3)_2Pb(SCN)_2I_2$ Single Crystals: Phase Transition and Moisture Stability. *ACS Appl. Mater. Interfaces* **2020**, *12*, 37713−37721.
74. Wang, S.; Yao, Y.; Wu, Z.; Peng, Y.; Li, L.; Luo, J. Realization of "warm" white light *via* halide substitution in polar two-dimensional hybrid perovskites $(2meptH_2)PbCl_xBr_{4-x}$. *J. Mater. Chem. C*, **2018**, *6*, 12267−12272.
75. Du, K.-Z.; Tu, Q.; Zhang, X.; Han, Q.; Liu, J.; Zauscher, S.; Mitzi, D. B. Two-dimensional lead(II) halide-based hybrid perovskites templated by acene alkylamines: crystal structures, optical properties, and piezoelectricity. *Inorg. Chem.* **2017**, *56*, 456−460.
76. Groom, C. R.; Bruno, I. J.; Lightfoot, M. P.; Ward, S. C. The Cambridge Structural Database. *Acta Cryst.* **2016**, *B72*, 171–179.
77. Marchenko, E. I.; Fateev, S. A.; Petrov, A. A.; Korolev, V. V.; Mitrofanov, A.; Petrov, A. V.; Goodilin, E. A.; Taraso, A. B. Database of Two-Dimensional Hybrid Perovskite Materials: Open-Access Collection of Crystal Structures, Band Gaps, and Atomic Partial Charges Predicted by Machine Learning. *Chem. Mater.* **2020**, *32*, 17, 7383–7388.
78. Billing, D. G.; Lemmerer, A. Synthesis, characterization and phase transitions in the inorganic-organic layered perovskite-type hybrids $[(C_nH_{2n+1}NH_3)_2PbI_4]$, n = 4, 5 and 6. *Acta Cryst.* **2007,** *B63*, 735–741.
79. Chen, X.-G.; Song, X.-J.; Zhang, Z.-X.; Li, P.-F.; Ge, J.-Z.; Tang, Y.-Y.; Gao, J.-X.; Zhang, W.-Y.; Fu, D.-W.; You, Y.-M.; Xiong, R.-G. Two-Dimensional Layered Perovskite Ferroelectric with Giant Piezoelectric Voltage Coefficient. *J. Am. Chem. Soc.* **2019**, *142*, 1077–1082.
80. Billing, D. G.; Lemmerer, A. Inorganic–organic hybrid materials incorporating primary cyclic ammonium cations: The lead bromide and chloride series. *CrystEngComm* **2009**, *11*, 1549–1562.
81. Billing, D. G.; Lemmerer, A. Synthesis and crystal structures of inorganic–organic hybrids incorporating an aromatic amine with a chiral functional group. *CrystEngComm* **2006**, *8*, 686–695.
82. Ye, H.-Y.; Liao, W.-Q.; Hu, C.-L.; Zhang, Y.; You, Y.-M.; Mao, J. G.; Li, P.-F.; Xiong, R.-G. Bandgap Engineering of Lead-Halide Perovskite-Type Ferroelectrics. *Adv. Mater.* **2016**, *28*, 2579–2586.
83. Yang, C.-K.; Chen, W.-N.; Ding, Y.-T.; Wang, J.; Rao, Y.; Liao, W.-Q.; Tang, Y.-Y.; Li, P.-F.; Wang, Z.-X.; Xiong, R.-G. The First 2D Homochiral Lead Iodide Perovskite Ferroelectrics: $[R\text{- and }S\text{-}1\text{-}(4\text{-Chlorophenyl})\text{ethylammonium}]_2PbI_4$. *Adv. Mater.* **2019**, *31*, 1808088.
84. Lemmerer, A.; Billing, D. G.; Synthesis, characterization and phase transitions of the inorganic–organic layered perovskite-type hybrids $[(C_nH_{2n+1}NH_3)_2PbI_4]$, n = 7, 8, 9 and 10. *Dalton Trans.* **2012**, *41*, 1146–1157.
85. Hong, Z.; Chong, W. K.; Ng, A. Y. R.; Li, M.; Ganguly, R.; Sum, T. C.; Soo, H. S. Hydrophobic Metal Halide Perovskites for Visible-Light Photoredox C−C Bond Cleavage and Dehydrogenation Catalysis. *Angew. Chem., Int. Ed*. **2019**, *58*, 456–460.
86. Ji, C.; Li, L.; Wang, S.; Han, S.; Peng, Y.; Zhang, S.; Luo, J. $(\gamma\text{-Methoxy propyl amine})_2PbBr_4$: a novel two-dimensional halide hybrid perovskite with efficient bluish white-light emission. *Inorg. Chem. Front.* **2021**, *8*, 2119–2124.
87. Jana, M. K.; Song, R.; Liu, H.; Khanal, D. R.; Janke, S. M.; Zhao, R.; Liu, C.; Vardeny, Z. V.; Blum, V.; Mitzi, D. B. Organic-to-inorganic structural chirality transfer in a 2D hybrid perovskite and impact on Rashba-Dresselhaus spin-orbit coupling. *Nature Commun.* **2020**, *11*, 4699.
88. Huang, P.-J.; Taniguchi, K.; Shigefuji, M.; Kobayashi, T.; Matsubara, M.; Sasagawa, T.; Sato, H.; Miyasaka, H. Chirality-Dependent Circular Photogalvanic Effect in Enantiomorphic 2D Organic–Inorganic Hybrid Perovskites. *Adv. Mater.* **2021**, *33*, 2008611.
89. Venkatesan, N. R.; Mahdi, A.; Barraza, B.; Wu, G.; Chabiny, M. L.; Seshadri, R. Enhanced yield-mobility products in hybrid halide Ruddlesden–Popper compounds with aromatic ammonium spacers. *Dalton Trans.* **2019**, *48*, 14019–14026.
90. Li, T.; Dunlap-Shohl, W. A.; Reinheimer, E. W.; Magueres, P. Le; Mitzi, D. B. Melting temperature suppression of layered hybrid lead halide perovskites via organic ammonium cation branching. *Chem. Sci. 2019*, **10**, 1168–1175.
91. Yangui, A.; Pillet, S.; Lusson, A.; Bendeif, E.-E.; Triki, S.; Abid, Y.; Boukheddaden, K. Control of the white-light emission in the mixed two-dimensional hybrid perovskites $(C_6H_{11}NH_3)_2[PbBr_{4-x}I_x]$. *J. Alloys Compd.* **2017**, *699*, 1122–1133.
92. Gong, X.; Voznyy, O.; Jain, A.; Liu, W.; Sabatini, R.; Piontkowski, Z.; Walters, G.; Bappi, G.; Nokhrin, S.; Bushuyev, O. et al. Electron–phonon interaction in efficient perovskite blue emitters. *Nature Mater*. **2018**, *17*, 550–556.
93. Sheikh, T.; Nag, A. Mn Doping in Centimeter-Sized Layered 2D Butylammonium Lead Bromide (BA_2PbBr_4) Single Crystals and Their Optical Properties. *J. Phys. Chem. C* **2019**, *123*, 9420–9427.
94. Wei, W.-J.; Li, C.; Li, L.-S.; Tang, Y.-Z.; Jiang, X.-X.; Lin, Z.-S. Phase transition, optical and dielectric properties regulated by

anion-substitution in a homologous series of 2D hybrid organic–inorganic perovskites. *J. Mater. Chem. C* **2019**, *7*, 11964–11971.
95. Mitzi, D. B. Synthesis, Crystal Structure, and Optical and Thermal Properties of $(C_4H_9NH_3)_2MI_4$ (M = Ge, Sn, Pb). *Chem. Mater*. **1996**, *8*, 791–800.
96. Calabrese, J.; Jones, N. L.; Harlow, R. L.; Herron, N.; Thorn, D. L.; Wang, Y. Preparation and characterization of layered lead halide compounds. *J. Am. Chem. Soc.* **1991**, *113*, 2328-2330.
97. Lemmerer, A.; Billing, D. G. Inorganic–Organic Hybrids Incorporating a Chiral Cyclic Ammonium Cation. *S. Afr. J. Chem.* **2013**, *66*, 262–272.
98. Passarelli, J. V.; Mauck, C. M.; Winslow, S. W.; Perkinson, C. F.; Bard, J. C.; Sai, H.; Williams, K. W.; Narayanan, A.; Fairfield, D. J.; Hendricks, M. P.; Tisdale, W. A.; Stupp, S. I. Tunable exciton binding energy in 2D hybrid layered perovskites through donor–acceptor interactions within the organic layer. *Nat. Chem*. **2020**, *12*, 672–682.
99. Lin, J.-T.; Chen, D.-G.; Yang, L.-S.; Lin, T.-C.; Liu, Y.-H.; Chao, Y.-C., Chou, P.-T.; Chiu, C.-W. Tuning the Circular Dichroism and Circular Polarized Luminescence Intensities of Chiral 2D Hybrid Organic–Inorganic Perovskites through Halogenation of the Organic Ions. *Angew. Chem., Int. Ed.* **2021**, *60*, 21434.
100. Oswald, W. H.; Koegel, A. A.; Neilson, J. R. General Synthesis Principles for Ruddlesden–Popper Hybrid Perovskite Halides from a Dynamic Equilibrium. *Chem. Mater.* **2018**, *30*, 8606–8614.
101. Adnan, M.; Rao, K. N.; Acharyya, J. N.; Kumar, D.; Dehury, K. M.; Prakash, G. V. Synthesis, Structural, Linear, and Nonlinear Optical Studies of Inorganic–Organic Hybrid Semiconductors $(R–C_6H_4CHCH_3NH_3)_2PbI_4$, (R = CH_3, Cl). *ACS Omega* **2020**, *4*, 19565.
102. Xie, G.; Wang, L.; Li, P.; Song, S.; Yao, C.; Wang, S.; Liu, Y.; Wang, Z.; Wang, X.; Tao, X. Low-Dimensional Hybrid Lead Iodide Perovskites Single Crystals via Bifunctional Amino Acid Cross-Linkage: Structural Diversity and Properties Controllability. *ACS Appl. Mater. Interfaces* **2021**, *13*, 3325–3335.
103. Mercier, N. $(HO_2C(CH_2)_3NH_3)_2(CH_3NH_3)Pb_2I_7$: a predicted non-centrosymmetrical structure built up from carboxylic acid supramolecular synthons and bilayer perovskite sheets. *CrystEngComm* **2005,** *7*, 429–432.
104. Jang, S.-H.; Kaminsky, W. CCDC 2016669: Experimental Crystal Structure Determination, **2020**.
105. Lemmerer, A.; Billing, D. G. Effect of heteroatoms in the inorganic–organic layered perovskite-type hybrids $[(ZC_nH_{2n}NH_3)_2PbI_4]$, n = 2, 3, 4, 5, 6; Z = OH, Br and I; and $[(H_3NC_2H_4S_2C_2H_4NH_3)PbI_4]$. *CrystEngComm* **2010**, *12*, 1290–1301.
106. Yao, J.; CCDC 1975113: Experimental Crystal Structure Determination, **2020**.
107. Yao, J.; CCDC 1883324: Experimental Crystal Structure Determination, **2018**.
108. Yao, J.; CCDC 1975109: Experimental Crystal Structure Determination, **2020.**
109. Jang, S.-H.; Kaminsky, W. CCDC 2016665: Experimental Crystal Structure Determination, **2020**.
110. Jang, S.-H.; Kaminsky, W. CCDC 2016667: Experimental Crystal Structure Determination, **2020**.
111. Hao, Y.; Wen, S.; Yao, J.; Wei, Z.; Zhang, X.; Jiang, Z.; Mei, Y.; Cai, H. *J. Solid State Chem.* **2019**, *270*, 226–230.
112. Zhang, H.-Y.; Song, X.-J.; Chen, X.-G.; Zhang, Z.-X.; You, Y.-M.; Tang, Y.-Y.; Xiong, R.-G. Observation of Vortex Domains in a Two-Dimensional Lead Iodide Perovskite Ferroelectric. *J. Am. Chem. Soc.* **2020**, *142*, 4925–4931.
113. Mercier, N.; Poiroux, S.; Riou, A.; Batail, P. Unique Hydrogen Bonding Correlating with a Reduced Band Gap and Phase Transition in the Hybrid Perovskites $(HO(CH_2)_2NH_3)_2PbX_4$ (X = I, Br). *Inorg. Chem.* **2004**, *43*, 8361–8366.
114. Smith, M. D.; Jaffe, A.; Dohner, E. R.; Lindenberg, A. M.; Karunadasa, H. I. Structural origins of broadband emission from layered Pb–Br hybrid perovskites. *Chem. Sci.* **2017**, *8*, 4497–4504.
115. Wang, Z.-X.; Liao, W.-Q.; Ye, H.-Y.; Zhang, Y. Sequential structural transitions with distinct dielectric responses in a layered perovskite organic–inorganic hyrid material: $[C_4H_9N]_2[PbBr_4]$. *Dalton Trans.* **2015**, *44*, 20406–20412.
116. Hoffman, J. M.; Malliakas, C. D.; Sidhik, S.; Hadar, I.; McClain, R.; Mohite, A. D.; Kanatzidis, M. G. Long periodic ripple in a 2D hybrid halide perovskite structure using branched organic spacers. *Chem. Sci.* **2020**, *11*, 12139–12148.
117. Kubicki, D. J.; Stranks, S. D.; Grey, C. P., Emsley, L. NMR spectroscopy probes microstructure, dynamics and doping of metal halide perovskites. *Nat. Rev. Chem.* **2021**, *5*, 624–645.
118. Lyu, R.; Moore, C. E.; Liu, T.; Yu, Y.; Wu, Y. Predictive Design Model for Low-Dimensional Organic–Inorganic Halide Perovskites Assisted by Machine Learning. *J. Am. Chem. Soc.* **2021**, *143*, 12766–12776.

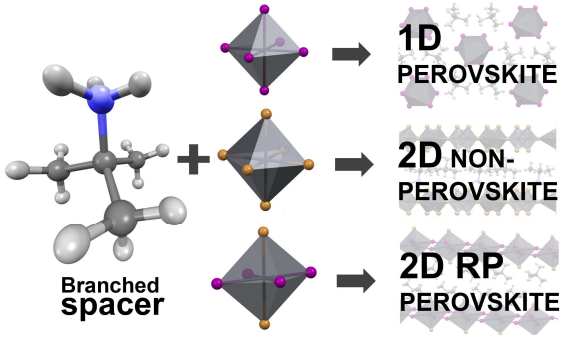
Branched
spacer
1D
PEROVSKITE
2D NON-
PEROVSKITE
2D RP
PEROVSKITE